

Solar Potential Assessment using Multi-Class Buildings Segmentation from Aerial Images

Hasan Nasrallah, Abed Ellatif Samhat^{*} Ghaleb Faour[†] Yilei Shi[‡] Ali J. Ghandour[§]

Abstract

Semantic Segmentation of buildings present in satellite images using encoder-decoder like convolutional neural networks is being achieved with relatively high pixel-wise metric scores. In this paper, we aim to exploit the power of fully convolutional neural networks for an instance segmentation task using extra added classes to the output along with the watershed processing technique to leverage better object-wise metric results. We also show that CutMix mixed data augmentations and the One-Cycle learning rate policy are greater regularization methods to achieve a better fit on the training data and increase performance. Furthermore, Mixed Precision Training provided more flexibility to experiment with bigger networks and batches while maintaining stability and convergence during training. We compare and show the effect of these additional changes throughout our whole pipeline to finally provide a set a tuned hyper-parameters that are proven to perform better.

1. Introduction

Building footprints extraction from aerial imagery is an important step for many urban applications including geographical databases, land use and change analysis among others. Fully automated extraction and recognition of building footprints and other urban objects such as roads and landmarks is a challenging problem.

The task of clustering parts of an image together which belong to the same object class is known as semantic image segmentation or pixel-level classification. Image segmentation can be treated as pixel-level prediction because it classifies each pixel into its category.

In this context, classifying pixels into semantic and instance objects in urban areas satellite images is currently

undergoing important attention in the research community, in addition to development efforts in the industry. This is because the remote sensing images are usually characterized by complex data in the form of heterogeneous regions with large intra-class variations and often lower inter-class variations [1]. Deep learning significantly reduces the time required to achieve such tasks due to its capabilities in automatically extracting meaningful and well defined features and patterns present in large scenes.

Deep Convolutional Neural Network (CNN) architecture is becoming prominent in earth observation applications. It consists of multiple interconnected layers and learns a hierarchical feature representation from raw pixel-data. CNN discovers features in multiple levels of representations.

The contribution of this paper is three-folds: (i) achieve instance segmentation using a single semantic segmentation network with an extra output channel and few post-processing modules, (ii) present a set of hyper-parameters optimization that can improve the overall accuracy of the network, (iii) present a new approach to analyze instance segmentation results visually using a Color-Map. We also compare the proposed method with other segmentation models [10, 17, 21] and show that it performs better.

The rest of the paper is organised as follows: Section 2 shows the literature review related to the use of deep learning models for building footprints detection from aerial images. We present in Section 3 the methodology adopted in the work. Then, deep learning model design is presented in Section 4. Study area is described in Section 5 and results are presented in Section 6. Finally, Section 8 concludes the paper.

2. Literature Review

Semantic Segmentation is the process of classifying every pixel present in an image to one or more predefined classes, while instance segmentation steps up the task to further group together the pixels belonging to the same object class.

There have been many methods proposed to solve the problem of building detection and segmentation from aerial imagery. Semantic segmentation networks [25] [16] [37]

^{*}H. Nasrallah and A. Samhat aew with the Lebanese University.

[†]A.J. Ghandour and G. Faour are with the National Center for Remote Sensing, at the National Council for Scientific Research (CNRS), Beirut, Lebanon.

[‡]Y. Shi is with the Technical University of Munich.

[§]Corresponding Author: A. J. Ghandour, aghandour@cnrs.edu

[4] are widely used nowadays to capture various features present in satellite images like ships [23] and buildings [28].

Most of the existing work in the literature uses fully Convolutional Neural Networks to achieve semantic segmentation at the pixel-level. The problem of instance segmentation is approached using more complex networks, composed of two stages usually, such as Region Proposal networks, Bounding Box Regressors, in addition to classifiers such as Fast and Faster-Region-based CNN (RCNN) [9] [24], Cascade-RCNN [3], and Efficient-Det [32].

The results on urban object detection in [26] indicated that buildings can be recognized and separated from the other terrain objects however, there is room for improvement towards the detection of small building structures and the precise delineation of building boundaries.

In [28], the authors use gated graph convolutional neural networks to output a Truncated Signed Distance Map (TSDM) which is then converted into a semantic segmentation mask of buildings. In [38], the authors use Mask-RCNN [10] to segment building instances and then apply a polygon border regularization process to regularize noisy building boundaries. In [20], the authors propose two plug and play modules to generate spatial augmented and channel augmented features for semantic segmentation from satellite images. In [15] the authors use augmentations like slicing, rescaling and rotations and additional GIS data to improve building footprint extraction. In [33], the authors use siamese networks to both segment and classify buildings present in pre and post disaster images. In [2], the authors perform instance segmentation using Fully Convolutional Neural Networks composed of a segmentation network followed by a Direction Net (DN) to predict the distance transform of every point from the border and finally a Watershed Transform Network (WTN) to predict the energy levels to be used in the watershed transform. However, a more direct approach is presented in [12] where the authors only use a segmentation network with an extra output mask designating the spacing between very close buildings to separate building instances.

3. Methodology

3.1. Model Architecture

UNet [25] is an end-to-end fully convolutional neural network that serves the purpose of semantic segmentation of input images over multiple classes. It consists of a contracting path [Encoder] and an expansive path [Decoder] with skip connections added between every two symmetrical blocks of same size in the encoder and the decoder. The Encoder is comprised of repeated down-sampling convolutional and pooling layers followed by an activation function at every stage (i.e. RELU) to output feature maps of higher semantics and lower resolution (half) from the pre-

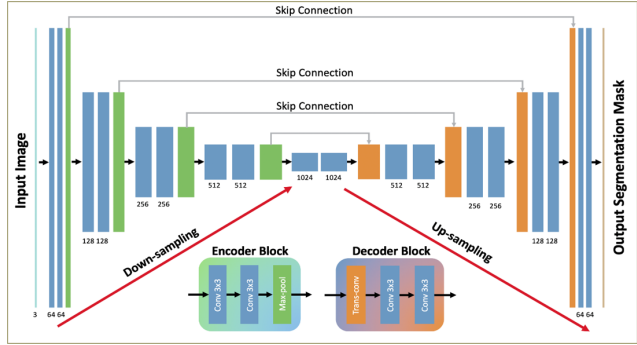


Figure 1. Encoder-Decoder UNet Architecture with Skip Connections

vious stage. Furthermore, the Decoder is made up of consecutive up-sampling blocks consisting of 3x3 convolution and an activation function followed by an up-sampling layer that doubles the resolution of the input maps. Each decoder block takes as input the output of the previous decoder block concatenated to the feature maps of same size from the parallel encoder block [skip connection]. Skip connections allow information to flow directly from the low level to high-level feature maps without alternations that even further improve localization accuracy and speed up convergence [12]. The selection of the activation function at the last decoder block depends on whether the output classes are dependent/independent and overlapping/non-overlapping, which will explain in later sections our choice of using the Sigmoid activation over the Softmax activation in our approach [22].

The overall is a U-shaped encoder-decoder architecture that takes an image as input, in our case 'RGB image', of size $H \times W$ and outputs a multi-channel map of same size where every channel designates a pixel-wise probability map for a certain class as shown in Figure 1. Typically, we choose a probability threshold (0.5 by default) to classify each pixel to a given class across all channels spatially.

The Encoder part of the architecture can be chosen from powerful and deep convolutional neural networks like Residual Nets [11, 34], Inception Nets [30], dual-path nets [5], or the newly introduced Efficient-Nets [31]. Efficient-Net-B0 is the baseline of a multi-objective neural architecture search that optimizes both accuracy and memory usage. Efficient-Nets-B1 to Efficient-Nets-B7 can be obtained using a compound scaling method. In our experiments, Efficient-Net-B3 was found to perform better in terms of accuracy and variance than other members of the Efficient-Net family members and other encoders like ResNet34, ResNeXt50, InceptionV4, InceptionResNetV2 and DPN92 as shown in Table 1, where distance is defined as the Fscore difference on the training and validation datasets. [31]

Backbone	FScore(%)	Distance(%)
ResNet34	82.8	4.33
ResNeXt50	83.7	4.24
Inception-ResNetV2	84.0	3.55
InceptionV4	84.1	4.95
DPN92	83.8	3.74
EfficientNetB2	83	2.93
EfficientNetB3	84.3	2.88
EfficientNetB4	83.8	2.97

Table 1. F-score and Distance percentages on the validation set using different backbones.

3.2. Loss Function

As for the loss function, we chose a normalized weighted sum of losses across all output channels. Each single channel loss is a combination of Dice loss and Binary Cross-Entropy loss [13] in order to leverage the benefits of both.

We calculate the loss per channel as a weighted combination of dice loss and binary cross entropy loss of this channel, so the loss for the i^{th} channel becomes:

$$L_i = \Gamma_1 * BCE_i + \Gamma_2 * Dice_i$$

where, for simplicity, let's assume that $\Gamma_1 = \Gamma_2 = 0.5$.

The Dice loss is used to measure the similarity between our model's prediction mask and the ground truth mask and is computed at a pixel level after calculating the total number of True Positive TP , False Positive FP and False Negative FN pixels as follows:

$$Dice = 1 - \frac{(1 + \beta^2) * TP + \epsilon}{(1 + \beta^2) * TP + \beta^2 * FN + FP + \epsilon}$$

where, $\beta = 1$ and $\epsilon = 0.0001$.

Binary Cross Entropy severely penalizes wrong predictions. This is crucial and mandatory for the model to learn to better classify buildings' border pixels. BCE is defined as follows:

$$BCE = \frac{1}{N} * \sum_{i=1}^N -(g_i * \log(p_i) + (1 - g_i) * \log(1 - p_i))$$

where N is the total number of pixels, g_i is the i^{th} pixel in the ground truth mask and p_i is the i^{th} pixel in the prediction mask.

We obtain the final loss for all channels by summing up all channel losses, each multiplied by the relative channel weight w_i across k -channels and normalized as follows:

$$TotalLoss = \frac{1}{\sum_{i=1}^k w_i} * \sum_{i=1}^k w_i * L_i$$

The optimization problem becomes to minimize this loss in order to maximize the pixel probabilities being classified to the right class.

4. Model Design

4.1. Training Pipeline

Our best model is trained over 100 epochs using Adam Optimizer [14] and the One-Cycle learning rate policy [29] starting with an initial learning rate = $\frac{0.0001}{20}$ and increases for 40 epochs in a cosine annealing manner till it reaches a maximum of 0.0001 and then decreases for the rest 60 epoch in the same annealing fashion to a much lower learning rate = $\frac{0.0001}{1000}$. When learning rate is high, the One-Cycle learning rate policy works as a regularization method and keep network from over-fitting.

Our GPU card is a Titan-Xp video card with 12GB of virtual RAM allowing us to train our model on a batch size of 10 512x512 pixel satellite images, however since this is a low batch size and the images are relevantly small, the model will see data of low diversity at each iteration, and thus we needed to utilize a higher batch size given our resources, so we used mixed precision training [19] where some operations like convolutions are performed over 16-bit instead of 32 saving up half the memory needed for these computations. We set the opt-level to 'O1' and used dynamic loss scaling. And hence, we were able to increase our batch size to 20 images, but we used a batch size = 16 since it provided slightly better results. Training our model for 100 epochs on our dataset takes about 2hrs, and we evaluate the performance over the validation set every epoch and save the weights of the best performing epoch's model on the validation set.

During training we apply randomly train time augmentations on images, where each image undergoes a series of augmentations. At random, the image first undergoes a positional transformation a probability equal to 0.8, then a color transform is applied with a probability equal to 0.7, then a distortion is added with a probability of 0.3, and finally we noise the image with a probability equal to 0.2. Each transformation block is a like a basket of equally likely augmentations. For instance, positional transformations include vertical or horizontal flips, 180 degree rotation and random-crop-resize augmentations. Color transformations include RGB-shifting, Random-Gamma and others...These train time augmentation are necessary to prevent high variance problems and to build a more robust model to changes and new data. Furthermore, we use CutMix [35] data augmentation to increase the intensity of our train time augmentations even more which is a regularization strategy to train a stronger model. Every batch of images undergoes this mixing of data where we align the list images together with a shuffled version of that list and crop out a random

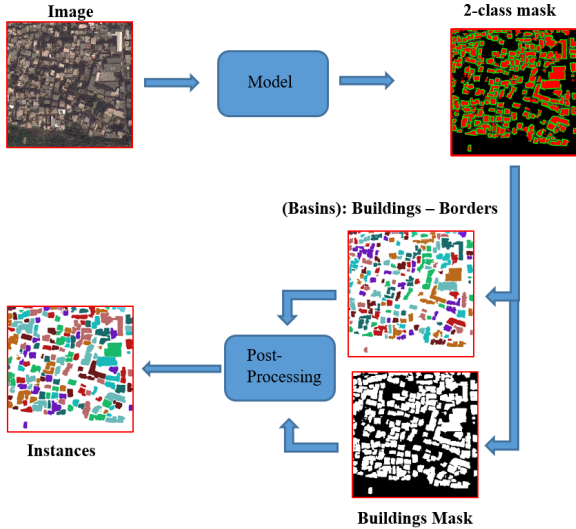


Figure 2. Post Processing Method

bounding box from the 2nd image and its corresponding label mask, and paste it in the 1st image.

4.2. Inference & Post Processing

At inference, each image undergoes 3 positional test-time augmentations (H-flip, V-flip, & 180° rotation so that the receptive fields of the model can view the same information in 4 different ways and then the output masks are simply averaged together. At the post processing step, we aim to convert our semantic segmentation task into an instance segmentation one, so for each image we take prediction mask and perform the following operation. For 1-class inference we simply extract the exteriors of all non-touching instances as polygons and filter out polygons having an area less than 140 pixels. For 2-class, we first subtract the borders mask from the buildings mask, in order to create the basins (or seed mask) for the watershed algorithm which designates the building nuclei (interiors). Given the seeds, the watershed processing matches each pixel present in the buildings mask to its corresponding basin (building nucleus). We obtain a mask with very well separated building footprint polygons by the watershed line. Each polygon is further tagged by a unique Id and polygons of area less than 140 pixels are discarded and considered as noise done by the model or by the post processing method. Figure 2 illustrates more about the post-processing method.

5. Study Area

Our aim in this research was to build an efficient and accurate building segmentation model to detect buildings in Lebanon from satellite images. So we chose a GeoTiff Im-

age covering the city of Tyre in the south of Lebanon as our training dataset. The dataset is a 35372x28874 GeoTiff image with RGB+NIR channels taken by the GeoEye-1 satellite sensors with a resolution of 50 cm/pixel. In our experiments we only used the optical channels to simplify the task and since optical data is more available than other types of radar and distance measures, this allows us to use our model for future purposes in case we lacked the existence of additional data.

To create our dataset we tiled our chosen GeoTiff image into 1024x1024 cropped images and removed the tiles containing no data [blank images]. We resulted with 338 image crops which we intended to label to complete our dataset. We used the VGG-Image-Annotator tool to manually label our images. The labelling process took about 100 hrs to label all the building rooftops present in these satellite images with precision and accuracy. The labelling process underwent a round of labelling and 2 rounds of careful checking and correction. We labelled building rooftops as polygons due to their irregular shapes. The labelled polygons are a sequence of connected x-y pixel coordinates relative to the top left corner of each image. Since 1024x1024 is a considered a large size for us to fit a sufficient number of images in memory at once and since our batch of images has to be of high diversity in order for the gradient calculation to be over a well representative sample of the dataset, we further cropped each image into 3 non-overlapping 512x512 sized images while preserving the relative labelled polygons indexes to each image. The final dataset is comprised of 1352 512x512 images. We labelled 9700+ buildings manually, with an average of 28 buildings per 1024x1024 pixel-images. Labelling took about 120 hours that involved two rounds of double checking for errors and correction. There is an average of 28 buildings per image. Figure 3 is a bar graph showing the number of images present in the dataset for each given range of building.

Finally, we automatically generate the ground truth border masks using Algorithm 1.

As for the test set we selected 30 1024x1024 Areas Of Interest (AOI) taken by the same satellite sensor from different cities in Lebanon like Beirut, Saida, Jounieh, Jbeil and Tripoli. This would help in assessing the generalizability of our model over the whole Lebanese geographical area. These AOI's contained dense urban regions (Beirut), organized urban regions (Saida), and some rural areas (Jbeil). These images are used for inference, and thus they are not included in the training process.

6. Experiments and Results

6.1. Automatic Mixed Precision

First, we test our performance when using Automatic Mixed Precision (AMP) training [19] instead of regular 32-

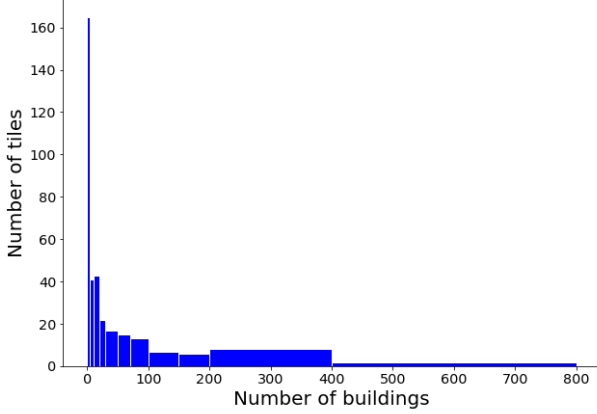


Figure 3. Number of 1024px Tiles per buildings count.

Algorithm 1 Border Mask Creation

- 1: Given a list of N Polygon Coordinates : $Polys = [P_1, P_2, \dots, P_N]$;
- 2: $H \leftarrow 1024$
- 3: $W \leftarrow 1024$
- 4: $AllBordersMask \leftarrow NumpyZerosArray((H, W)) \triangleright H \times W$ array of zeros
- 5: **for** P in $Polys$ **do**
- 6: $TempMask \leftarrow NumpyZerosArray((H, W))$
- 7: Draw & Fill Polygon P in $Temp$ with ones
- 8: $N \leftarrow 2$
- 9: $ker \leftarrow Square(3)$
- 10: $ErodedMask \leftarrow Erosion(TempMask, N, ker)$
 \triangleright Perform Binary Erosion on the Temporary Mask with a 3×3 squared kernel for $N=2$ times
- 11: $CurrentBorderMask \leftarrow Temp \oplus Eroded$ \triangleright XOR operation get the border mask of Polygon P
- 12: Extract Border pixels coordinates from $CurrentBorderMask$ & assign ones to these coordinates in $AllBordersMask$
- 13: **end for**

bit fixed precision training. Our results show that when using AMP training we are able to free up enough memory space enabling us to fit EfficientNet-B4 instead of EfficientNet-B2 (as Encoder) while preserving same batch size of 12 images, however later experiments proved that AMP training using EfficientNet-B3 UNet Model and a batch size of 16 images provides better results as shown in Figure 4.

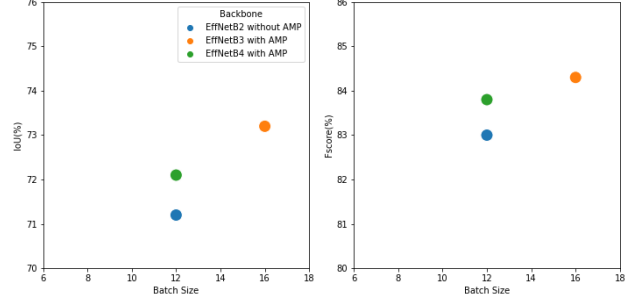


Figure 4. IoU's and Fscore's on Validation Dataset vs Batch Size for each EfficientNet encoder and AMP usage

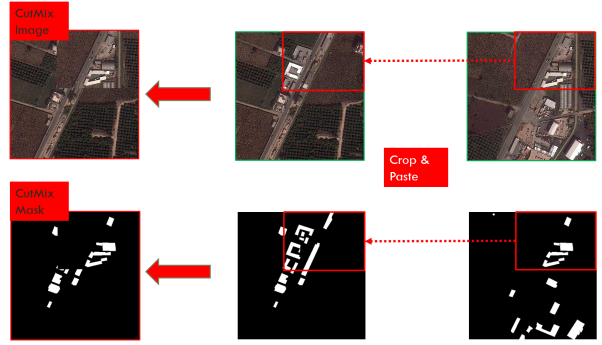


Figure 5. CutMix Image and Mask Creation: A random bounding box is cropped from first image and pasted in the second Image.

6.2. Mixed Data Augmentations

We further inspected the effect of mixed data augmentations like Cutmix [35] and MixUp [36]. CutMix was introduced in [35] and used for classification purpose where the truth label becomes a weighted combination of two classes. In our case, for segmentation purposes, we create the masks in the same fashion that the images are created as shown in Figure 5.

When using Cutmix, our IoU score increased from 73.2% to 75.1% and our Fscore increased from 84.3% to 85.6%. We also show that the distance between the Train and Validation scores decreases to approximately half when using CutMix which shows that a better fit is obtained. However, Using Mixup lead to poorer results as our IoU and Fscore decreased to 71.6% and 83.8% respectively.

6.3. Learning Rate

In previous experiments, we used Polynomial learning Rate that was first proposed in [37], where we decayed the learning rate from the initial one of 0.001 according to the formula : $lr_{t+1} = lr_t * (1 - \frac{epoch_{current}}{epoch_{max}})^{0.9}$, however we also tried Cyclical

Learning rate [27] with 5 cycles per 100 epochs, Cyclical Learning Rate with Warm Restarts [18] with $T_0 = 1$ and $T_{mul} = 2$, and super convergence using one cycle learning rate policy [29] as described in section 4.1. We obtain that the latter outperforms all by a margin as shown in Table 2 below that summarizes all our experiments.

6.4. Multi-class Segmentation

Since Semantic Segmentation often poorly classifies pixels present at the boundaries of touching objects present in an image, this may not be problem if we are assessing our results at a pixel level since the number of border pixels is much lower than that of object pixels, but it is surely a problem if we want to extract instances from our semantic masks by treating each non-intersecting segment as a separate instance. So we added an extra output channel designating the border pixels of the buildings. This way we are able to better separate very close buildings apart and identify each building instance correctly. To train our 2-class model we used for each channel a weighted loss $loss_{channel} = 0.5 * Dice + 0.5 * BCE$, and a $TotalLoss = \frac{1}{\alpha + \beta} * (\alpha * loss_{buildings} + \beta * loss_{borders})$, where $\alpha = 1$ and β was varied until we achieved the nearest Building pixel Fscore to our 1-class model. As shown in Table 3 below, we achieved best results a value $\beta = 2$ where $Fscore = 85\%$.

The real comparison between 1-class model and 2-class model is however at an object level, so in order to fairly compare between the two methods at inference time we used the F1Score or the SpaceNet Buildings Metric [8].

As described in section 4.2, the raw results of a 2-class model are processed using the watershed processing algorithm with the buildings interiors as seed mask. Building interiors is the result of the subtraction of the buildings mask from the boundaries mask. This watershed post-processing outputs an instance mask where each building is tagged with a unique number as shown in Figure 6.

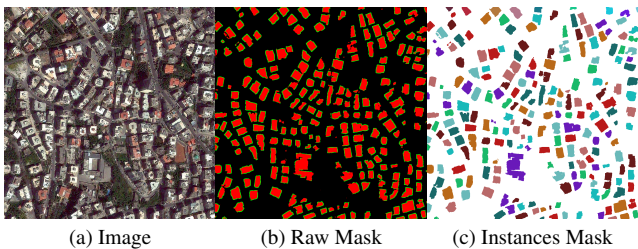


Figure 6. 2-class inference: A satellite image with its corresponding raw 2-Class Mask prediction and a Mask of separate Building Instances after applying the watershed transform. Building instances are shown in different colors

Mainly, we run object level scoring over the same test set we used to score our semantic segmentation performance.

We calculate the total number of True Positives, False Positives, False Negatives for every test image and then the F1Score is calculated globally over all images to measure our overall performance as shown in Table 4.

We also sampled various tiles from different regions in Lebanon including Beirut, Saida, Jounieh/Jbeil and Tripoli for which we ran the two pipelines and calculated the obtained scores as shown in Table 5.

Results in Table 5 show that the 2-class model approach provides up to 14% increase in F1Score. The Nadir angle for very dense areas with tall buildings, like Beirut, is a major factor that affects the semantic segmentation, and hence the instance, as the model tends to classify building’s walls which damages the IoU score when computing the instance segmentation metric. This explains why the F1Score dropped over satellite images taken from the capital city, given the fact that the model wasn’t trained ultra-dense areas with very tall buildings. We can ensure an F1Score above 66% for other regions, and for very organized cities like Saida our model can provide predictions with a an outstanding F1 of values higher than 80%.

Furthermore, In order to further investigate the performance per image for the 1-class and 2-class methods, we draw the violin plots in Figure 7 to compare the probability density for the number of TP-FP-FN predictions per each image on the test dataset. The dashed line represent the median of each distribution and the dotted lines represent the interquartile ranges (IQR). IQR represents the ‘Middle 50%’ distribution of the data, so its a measure of where the bulk in the values is in. We aim on one hand to increase the number of TP per image and the on the other to decrease FP and TN per image. The blue and orange violin plots designating the 1-class and 2-class model distributions show that for the same set of images, the medians and the IQR boundaries of the True Positive plots are higher for the output results of the 2-class model, and that the same values of False Positive and False Negative plots are lower in favour of the 2-class model. The fact that the data spread of these output results are in favour of the 2-class model approach show that this method out-performs at test time.

Finally, we also compare our 2-class model with other (semantic/instance) segmentation benchmark models as shown in Table 6, where we show that the proposed model outperforms by a margin at object-level. The same post-processing pipeline was adapted for semantic segmentation models [FCN-8s [17] and B-FCN [21]] for a fair comparison. Mask-RCNN [10] on the other hand required 3X times more iterations (300 epochs) than other semantic segmentation models. The proposed model showed on average a 10% F1-score improvement over the 2nd best performing model.

N	Backbone	AMP	Mixed Augs	Scheduler	Fscore
1	EffNet-B2	✗	✗	PolyLr	83
2	EffNet-B3	✓	✗	PolyLr	84.3
3	EffNet-B4	✓	✗	PolyLr	83.8
4	EffNet-B3	✓	MixUp	PolyLr	83.2
5	EffNet-B3	✓	CutMix	PolyLr	85.6
6	EffNet-B3	✓	CutMix	CycLR	85.2
7	EffNet-B3	✓	CutMix	CycLR WM	85.2
8	EffNet-B3	✓	CutMix	1Cycle	87.6

Table 2. Pixel Fscore results on our validation dataset showing a series of improvements done by searching for the best hyper-parameters like backbone architecture, automatic mixed precision, mixed augmentation and learning rate schedulers.

β	Buildings Fscore	Borders Fscore
0.1	83.3	53
0.25	83.7	53.9
0.5	83.8	54.3
1.0	83.8	55.1
2.0	84.8	55.3
5.0	84	55.5

Table 3. Fscore results computed per building and border channels for each given value of β used as the weight multiplied to the border channel loss in the overall loss function.

Model	TP	FP	FN	F1Score(%)
1-Class	711	400	1009	50.22
2-Class	1100	506	620	66.14

Table 4. True Positive, False Positive and False Negative Counts with the corresponding F1Score as Instance Segmentation Metrics on the Validation dataset, show the superiority of the 2-Class Model over the 1-Class Model.

Region	1-class F1Score(%)	2-class F1Score(%)
Saida	67.40	81.56
Tripoli	56.15	70.20
Jounieh/Jbeil	56.68	67.03
Beirut	49.07	55.10

Table 5. A comparison between 1-Class and 2-Class methods F1score results on images from different regions in our Test Dataset.



Figure 7. Violin Plots showing the True Positive, False Positive and False Negative probability density distributions to compare the instance segmentation performance between the 2 methods.

Model	Region F1-Score(%)			
	Saida	Tripoli	Jounieh-Jbeil	Beirut
Mask-RCNN [10]	66.5	59.6	58.8	42.7
B-FCN [21]	67.8	47.1	54.1	48.1
FCN-8s [17]	71.75	58.42	57.1	47.9
Ours	81.56	70.2	67.03	55.1

Table 6. A comparison between Our 2-class Unet Model and other segmentation models. We adapt the same post-processing for semantic segmentation models for a fair comparison.

6.5. Color-Map

To better Visualize our Results and to shed the light on the problems that the 2-class model approach helped to resolve in a non-numerical way, we made a color map that indicates whether the predicted polygons are True Positives or False Positives and to check which ground truth polygons were left out (False Negatives). So we associated the TPs, FPs, and FNs with the colors 'Red', 'Green' and 'Blue'.

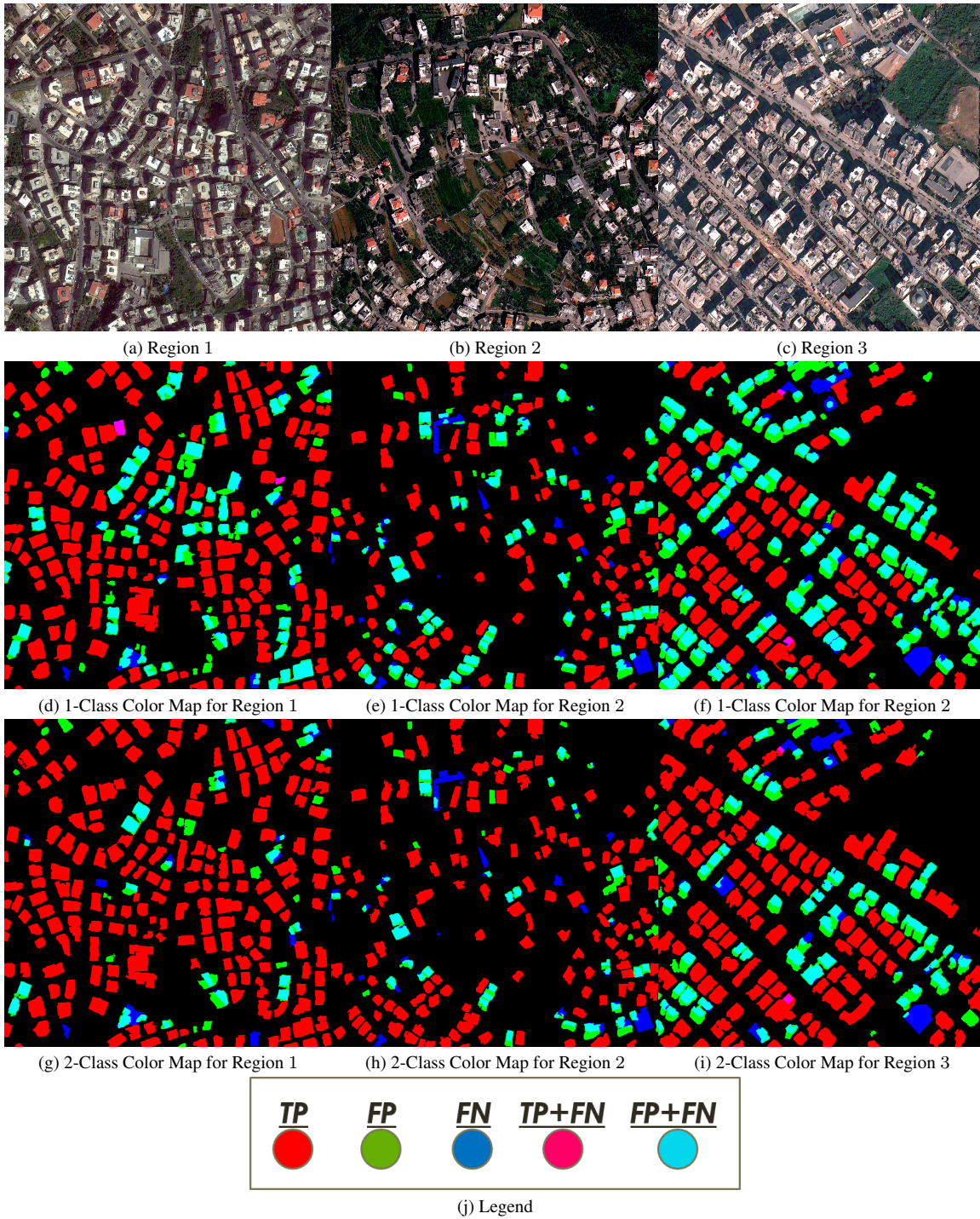


Figure 8. Three image regions with their corresponding True Positive, False Positive, False Negative Color Maps and the needed Legend.

However, since there are cases where we might encounter an overlap between these attributes, the 'Cyan' color (Overlap between FP and FN) and the 'Magenta' color (Overlap between TP and FN) are also part of this color-mapping, and

since there cannot be an overlap between TPs and FPs in this instance segmentation task, the 'Yellow' color is never a valid case and therefore 'White' too.

The main reason for using this color topology is to vi-

sualize the differences between the prediction of the two methods under study, as we would like to obtain a more red-dish prediction mask where the number of True Positives is dominant. As is shown in Figure 8 where the prediction’s TP/FP/FN color-map for 2-classes model clearly shows the superiority in performance over the 1-class model. For instance in Figure 8, the 2-classes model was able to detect 32 more True Positive building footprints than the 1-class model approach. Cyan color indicates the a Positively detected building polygon has a highest $IoU < 0.5$ amongst all ground truth building footprint. This problem arises when (1) a prediction polygon represents an under-segmented building footprint or (2) a prediction polygon merges two or more building footprints together. As shown in the Figure 8 that (2) is mostly the case, so the 2-model’s approach solves the problem of merging very close buildings together and classifying them as a single building. Magenta on the other hand, although less frequent, indicates that a prediction polygon extends to contain more than one building footprint while preserving an $IoU \geq 0.5$ with a certain ground truth building footprint, and this mainly occurs when one of the merged/predicted buildings is of an area much larger than the combined area of the others not allowing the IoU to drop below 0.5. These visualizations show the the additional border segmentation and the watershed post-processing helped in better separating and segmenting building instances by reducing the error done between adjacent footprints.

In this way, we can conclude that the 2-class model approach resolved the problems occurring at the boundaries of very close buildings that result in merging 2 or more building footprints as a single one.

7. Solar Potential Application

In this section, we will discuss how we utilized the generated buildings footprints in order to calculate the solar potential per year of rooftops over all Lebanon. In order to calculate the solar potential of each rooftop, we first have to place solar panels within the designated area of the extracted building footprints . After placing the solar panels, we will then have information about how many solar panels can fit in each roof. Finally we use the following formula to calculate the solar potential of every rooftop:

$$SolarPotential(MWh/year) = N_{panels} * P_{nominal} * PV_{out}$$

Where N_{panels} is the number of panels placed on the roof, $P_{nominal}$ is the maximum power of the solar panel module in (KWp), and PV_{out} is the specific photovoltaic power in (MWh/KWp)

7.1. Solar Panels Placement

The first step in calculating the solar potential of rooftops, is to find how many solar panels can fit in each

roof. But since we lack information like the relative slope and azimuth angle of each rooftop, we assume that the roofs are flat and at an orthogonal angle with the satellite sensor. Other Factors like shading are also not taken into consideration due to insufficient knowledge of the building heights. We use a standard commercial type of solar panel modules of dimensions (1x1.98) meters and a nominal power $P_{nominal} = 0.4$ KWp. Simply dividing the area of the rooftop by the area of the module does not take the rooftop’s morphology into account and thus it is not accurate enough. We use an algorithm to place the panels similar the one proposed here [6] as follows:

For each building footprint polygon, we find its minimum bounding rectangle. Then we designate the rectangle’s longest axis as the main axis of the rooftop. The solar panels are placed in a greedy way next to each other in the rectangle along the main axis. Finally we remove the solar panels that extend out of the original rooftop polygon geometry. The whole process is shown in Figure9.

7.2. Solar Potential Map

PV_{out} data were obtained from the “Global Solar Atlas 2.0”, a free, web-based application that utilizes SolarGIS data. We obtain a 240x360 pixel GeoTIF image/map of resolution (0.0083x0.0083), where an average yearly PV_{out} is calculated over $N \times N m^2$ tiles. For every rooftop, we locate the corresponding tile it lies within in the PV_{out} map to obtain its relative PV_{out} value in (MWh/KWp). Thus we base our calculation on more accurate and precise PV_{out} map than other studies [7], where they use a fixed value over the entire city. The PV_{out} heatmap is shown in Figure 10.

Finally, we proceed on calculating the solar potential of every building rooftop based on the equation stated in the introduction of this section. For every rooftop we count the number of placed solar panels and locate the specific tile it belongs to in the PV_{out} map to obtain its relative PV_{out} value. Since we use a greedy algorithm for the solar panels placement, this results in over-placement of these modules on the roof. In reality, less solar panels could be placed on the rooftop due to some obstacles or the inclined slope of the surface. So we further multiply the number of solar panels with ratios [0.1, 0.25 ,0.5, 0.75] for comparison and to obtain more realistic results, because in reality less than 75% of these greedily placed panels could be really placed on the roof. Figure 11 shows how every rooftop is assigned a specific solar potential value.

For every district, we calculate the total solar potential (GWh) and the average solar potential produced by the rooftops(MWh) of its buildings. Figure 12 shows these produced maps. From map(a), we can show that Beirut and Tripoli Districts maintain the highest average solar potential per rooftop (92 and 70 (MWh/year)) respectively if 50% of solar panels were placed. This reflects the fact that

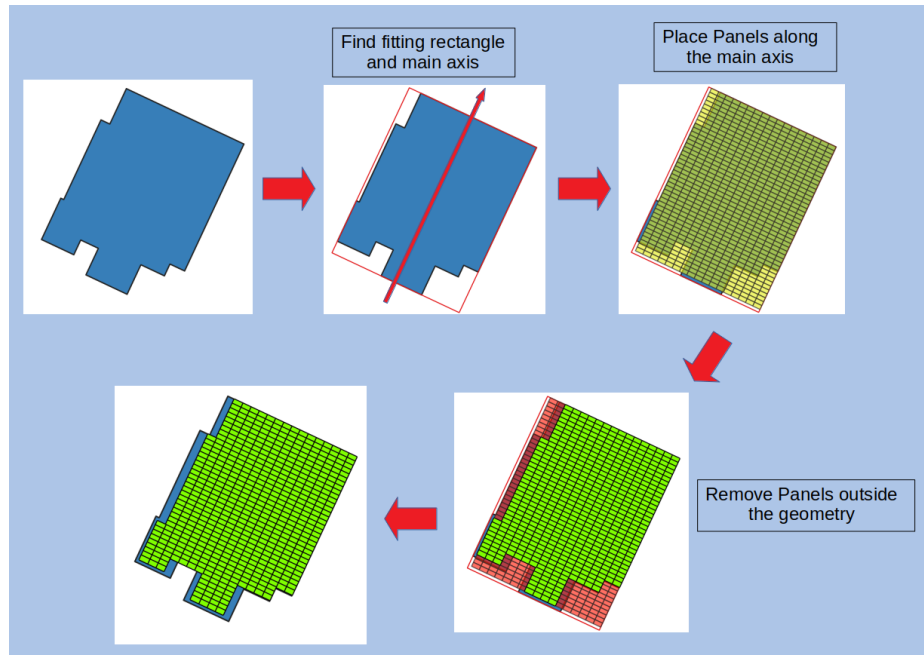


Figure 9. Solar Panels Placement Algorithm

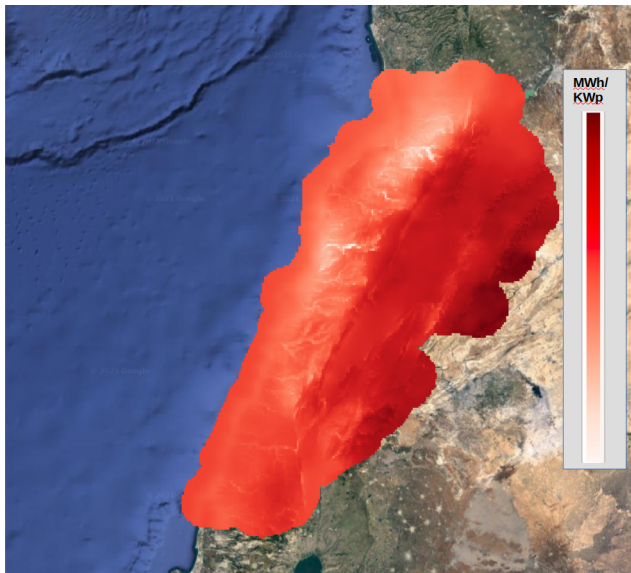


Figure 10. PV_{out} heatmap

the rooftops in these district have higher relative areas that other districts. However as shown in Figure 14, these areas contribute to the most glowing regions indicating a high average solar potential per $4Km^2$ which is due to the high building density present. If effects like shadowing were taken into consideration, we expect a lower average solar

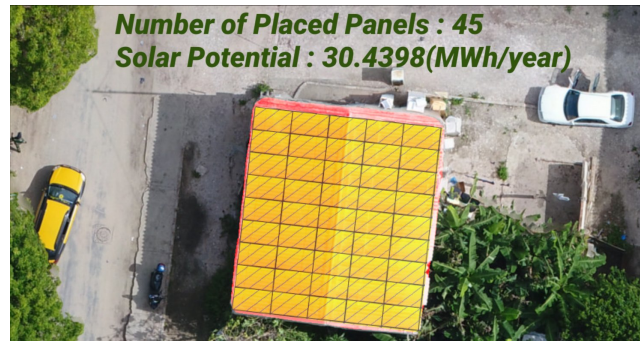


Figure 11. Solar Potential Value for a given rooftop after solar panel placement.

potential in these high density districts. Map(b) shows that districts like Baalbeck, Zahle and Akkar have the highest total solar potentials (2885, 1979 and 1775 ($GWh/year$)) despite holding a low average solar potential value per building. Now these mentioned districts contain vast unpopulated areas which makes them capable of producing even more solar energy. We also infer from districts having both low average and total solar potential like Hermel, Hasbaya and Jezzine, that their areas are not utilized properly and we can take advantage of their void spaces for solar energy production.

We also show the number of buildings for each solar potential range if 50% of solar panels were placed in Figure

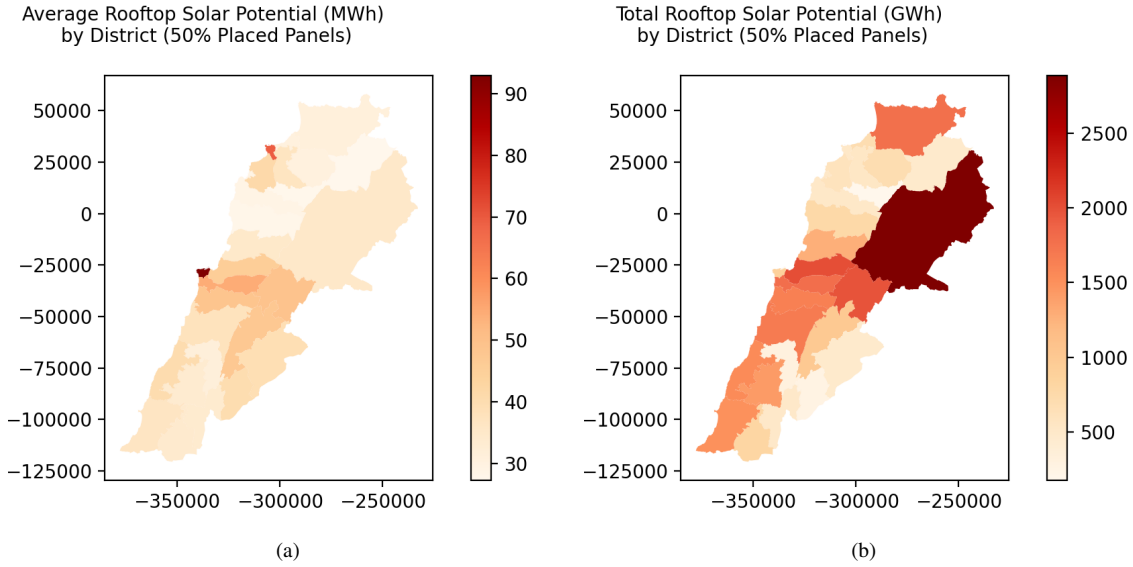


Figure 12. Average and Total Solar Potential Maps By District

13. We deduce that one can expect that his rooftop can produce a solar potential up-to $100(MWh/year)$ if he places 50%. Rooftops with higher solar potential are a rare case, and mainly values above $350(MWh/year)$ are due to segmentation errors in high dense areas like slums. The distribution even shows that rooftops with lower solar potentials (up to $10(MWh/year)$) correspond to more than $120K$ detected buildings of supposedly small roof areas considering that PV_{out} is nearly uniform in Lebanon as shown in Figure 10.

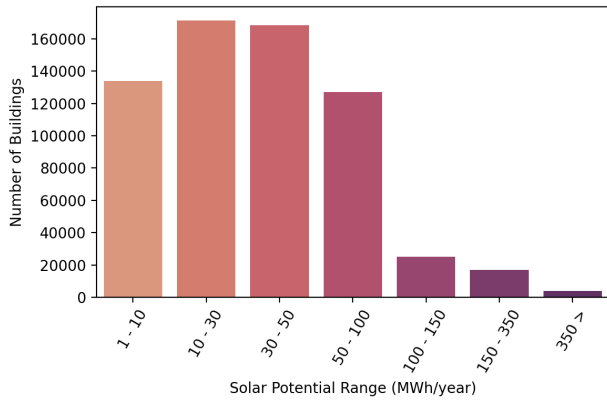


Figure 13. Building Count for Every Solar Potential Range.

Figure 14 visualizes a heatmap of the total solar potential in $(MWh/year)$ for every $4Km^2$ tile. Rather than inspecting the orange/yellowish rare parts of the map, we should take into consideration the nearly uniformly blue huge part

in north Lebanon. This part of low average solar potential also holds a darker red color in the PV_{out} map (Figure 10) than most of the other regions which indicates a higher PV_{out} value. The fact that this area belongs to the western Lebanese mountain range(needs discussion to continue)....

Heatmap showing the Total Solar Potential (MWh/year) per $4Km^2$

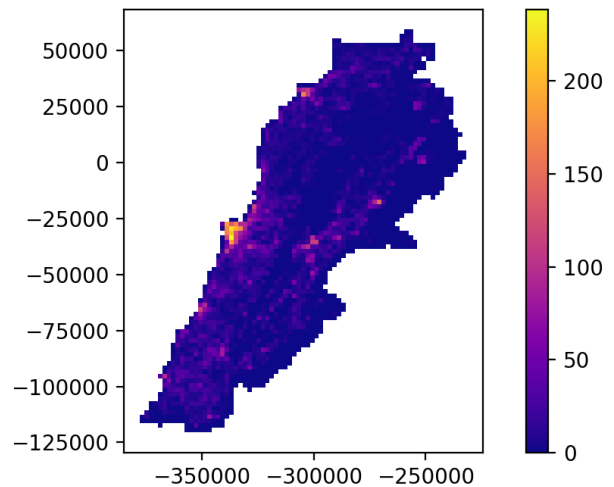


Figure 14. Heatmap showing the Total Solar Potential (MWh/year) per $4Km^2$ when placing 50% of solar panels on the rooftops

We also show the Table 7 the total solar potential

(GWh/year) for every district given a percentage of solar panels that can be placed on the rooftops the greedy algorithm. In reality it is not feasible to place 100% of the proposed solar panels.

8. Conclusion

In this paper we presented a 2-Class Model approach used for the instance segmentation of building present in satellite images. We showed how mixed precision training, mixed data augmentations and the use of efficient nets as feature extractors can improve our semantic segmentation performance. We further presented and discussed how the watershed post-processing technique aid in resolving instance segmentation errors at the boundaries by showing that visually using our original TP/FP/FN color map.

References

- [1] Rasha Alshehhi, Prashanth Reddy Marpu, Wei Lee Woon, and Mauro Dalla Mura. Simultaneous extraction of roads and buildings in remote sensing imagery with convolutional neural networks. *ISPRS Journal of Photogrammetry and Remote Sensing*, 130:139 – 149, 2017. [1](#)
- [2] M. Bai and R. Urtasun. Deep watershed transform for instance segmentation. In *2017 IEEE Conference on Computer Vision and Pattern Recognition (CVPR)*, pages 2858–2866, 2017. [2](#)
- [3] Zhaowei Cai and N. Vasconcelos. Cascade r-cnn: Delving into high quality object detection. *2018 IEEE/CVF Conference on Computer Vision and Pattern Recognition*, pages 6154–6162, 2018. [2](#)
- [4] Liang-Chieh Chen, George Papandreou, Florian Schroff, and Hartwig Adam. Rethinking Atrous Convolution for Semantic Image Segmentation. *arXiv e-prints*, page arXiv:1706.05587, June 2017. [2](#)
- [5] Y. Chen, J. Li, H. Xiao, X. Jin, S. Yan, and Jiashi Feng. Dual path networks. In *NIPS*, 2017. [2](#)
- [6] Daniel de Barros Soares, François ANDRIEUX, Bastien HELL, Julien LENHARDT, JORDI BADOSA, Sylvain GAVOILLE, Stéphane GAUFFAS, and Emmanuel BACRY. Predicting the solar potential of rooftops using image segmentation and structured data. In *NeurIPS 2020 Workshop on Tackling Climate Change with Machine Learning*, 2020. [9](#)
- [7] Hossein Eslami, Sara Najem, Dana Abi Ghanem, and Ali Ahmad. The potential of urban distributed solar energy in transition economies: The case of beirut city. *Journal of Environmental Management*, 285:112121, 2021. [9](#)
- [8] Adam Van Etten, Dave Lindenbaum, and Todd M. Bacastow. Spacenet: A remote sensing dataset and challenge series. *CoRR*, abs/1807.01232, 2018. [6](#)
- [9] R. Girshick. Fast r-cnn. In *2015 IEEE International Conference on Computer Vision (ICCV)*, pages 1440–1448, 2015. [2](#)
- [10] K. He, G. Gkioxari, P. Dollár, and R. Girshick. Mask r-cnn. *IEEE Transactions on Pattern Analysis and Machine Intelligence*, 42(2):386–397, 2020. [1](#), [2](#), [6](#), [7](#)
- [11] K. He, X. Zhang, S. Ren, and J. Sun. Deep residual learning for image recognition. In *2016 IEEE Conference on Computer Vision and Pattern Recognition (CVPR)*, pages 770–778, 2016. [2](#)
- [12] Vladimir Iglovikov, Selim Seferbekov, Alexander Buslaev, and Alexey Shvets. Terausnetv2: Fully convolutional network for instance segmentation. In *The IEEE Conference on Computer Vision and Pattern Recognition (CVPR) Workshops*, June 2018. [2](#)
- [13] S. Jadon. A survey of loss functions for semantic segmentation. In *2020 IEEE Conference on Computational Intelligence in Bioinformatics and Computational Biology (CIBCB)*, pages 1–7, 2020. [3](#)
- [14] Diederik P. Kingma and Jimmy Ba. Adam: A method for stochastic optimization. *CoRR*, abs/1412.6980, 2015. [3](#)
- [15] Weijia Li, Conghui He, Jiarui Fang, Juepeng Zheng, Hao-huan Fu, and Le Yu. Semantic segmentation-based building footprint extraction using very high-resolution satellite images and multi-source gis data. *Remote Sensing*, 11(4), 2019. [2](#)
- [16] T. Lin, P. Dollár, R. Girshick, K. He, B. Hariharan, and S. Belongie. Feature pyramid networks for object detection. In *2017 IEEE Conference on Computer Vision and Pattern Recognition (CVPR)*, pages 936–944, 2017. [1](#)
- [17] J. Long, E. Shelhamer, and T. Darrell. Fully convolutional networks for semantic segmentation. In *2015 IEEE Conference on Computer Vision and Pattern Recognition (CVPR)*, pages 3431–3440, 2015. [1](#), [6](#), [7](#)
- [18] Ilya Loshchilov and Frank Hutter. SGDR: stochastic gradient descent with warm restarts. In *5th International Conference on Learning Representations, ICLR 2017, Toulon, France, April 24-26, 2017, Conference Track Proceedings*. OpenReview.net, 2017. [6](#)
- [19] Paulius Micikevicius, Sharan Narang, Jonah Alben, Gregory Diamos, Erich Elsen, David Garcia, Boris Ginsburg, Michael Houston, Oleksii Kuchaiev, Ganesh Venkatesh, and Hao Wu. Mixed precision training. In *International Conference on Learning Representations*, 2018. [3](#), [4](#)
- [20] Lichao Mou, Yuansheng Hua, and Xiao Xiang Zhu. A relation-augmented fully convolutional network for semantic segmentation in aerial scenes. In *Proceedings of the IEEE/CVF Conference on Computer Vision and Pattern Recognition (CVPR)*, June 2019. [2](#)
- [21] L. Mou and X. X. Zhu. Vehicle instance segmentation from aerial image and video using a multitask learning residual fully convolutional network. *IEEE Transactions on Geoscience and Remote Sensing*, 56(11):6699–6711, 2018. [1](#), [6](#), [7](#)
- [22] Chigozie Nwankpa, W. Ijomah, A. Gachagan, and S. Marshall. Activation functions: Comparison of trends in practice and research for deep learning. *ArXiv*, abs/1811.03378, 2018. [2](#)
- [23] Venkatesh R and Anand Metha. Segmenting ships in satellite imagery with squeeze and excitation u-net. *CoRR*, abs/1910.12206, 2019. [2](#)
- [24] Shaoqing Ren, Kaiming He, Ross Girshick, and Jian Sun. Faster r-cnn: Towards real-time object detection with region

District	Panels(%)	Total Solar Potential (GWh/year)				
		100%	75%	50%	25%	10%
Baalbek		5771	4328	2885	1442	577
El Metn		4029	3022	2014	1007	402
Zahlé		3958	2968	1979	989	395
Baabda		3572	2679	1786	893	357
Akkar		3550	2662	1775	887	355
Chouf		3359	2519	1679	839	335
Aley		3282	2461	1641	820	328
Saida		3095	2321	1547	773	309
Sour		3006	2255	1503	751	300
Nabatiyé		2860	2145	1430	715	286
Kesrouane		2556	1917	1278	639	255
Békaa Ouest		2019	1514	1009	504	201
Beyrouth		1814	1360	907	453	181
Bent Jbail		1637	1227	818	409	163
Jbail		1556	1167	778	389	155
Minié-Danniyé		1409	1057	704	352	140
Koura		1206	904	603	301	120
Zgharta		1079	809	539	269	107
Batroun		1046	784	523	261	104
Tripoli		1032	774	516	258	103
Marjayoun		1017	762	508	254	101
Hermel		959	719	479	239	95
Rachaiya		954	716	477	238	95
Jezzine		623	467	311	155	62
Hasbaiya		532	399	266	133	53
Bcharré		353	265	176	88	35

Table 7. Total Solar Potential($GWh/year$) per district for different percentages of placed solar panels.

- proposal networks. In C. Cortes, N. Lawrence, D. Lee, M. Sugiyama, and R. Garnett, editors, *Advances in Neural Information Processing Systems*, volume 28. Curran Associates, Inc., 2015. 2
- [25] Olaf Ronneberger, Philipp Fischer, and Thomas Brox. U-net: Convolutional networks for biomedical image segmentation. In Nassir Navab, Joachim Hornegger, William M. Wells, and Alejandro F. Frangi, editors, *Medical Image Computing and Computer-Assisted Intervention – MICCAI 2015*, pages 234–241, Cham, 2015. Springer International Publishing. 1, 2
- [26] Franz Rottensteiner, Gunho Sohn, Markus Gerke, Jan Dirk Wegner, Uwe Breitkopf, and Jaewook Jung. Results of the isprs benchmark on urban object detection and 3d building reconstruction. *ISPRS Journal of Photogrammetry and Remote Sensing*, 93:256 – 271, 2014. 2
- [27] Tom Schaul, Sixin Zhang, and Yann LeCun. No more pesky learning rates. In Sanjoy Dasgupta and David McAllester, editors, *Proceedings of the 30th International Conference on Machine Learning*, volume 28 of *Proceedings of Machine Learning Research*, pages 343–351, Atlanta, Georgia, USA, 17–19 Jun 2013. PMLR. 6
- [28] Y. Shi, Q. Li, and X. X. Zhu. Building extraction by gated graph convolutional neural network with deep structured feature embedding. In *IGARSS 2020 - 2020 IEEE International Geoscience and Remote Sensing Symposium*, pages 3509–3512, 2020. 2
- [29] Leslie N. Smith and Nicholay Topin. Super-Convergence: Very Fast Training of Neural Networks Using Large Learning Rates. *arXiv e-prints*, page arXiv:1708.07120, Aug. 2017. 3, 6
- [30] Christian Szegedy, Sergey Ioffe, Vincent Vanhoucke, and Alexander A. Alemi. Inception-v4, inception-resnet and the impact of residual connections on learning. In *Proceedings of the Thirty-First AAAI Conference on Artificial Intelligence*, AAAI’17, page 4278–4284. AAAI Press, 2017. 2
- [31] Mingxing Tan and Quoc Le. EfficientNet: Rethinking model scaling for convolutional neural networks. In Kamalika Chaudhuri and Ruslan Salakhutdinov, editors, *Proceedings of the 36th International Conference on Machine Learning*, volume 97 of *Proceedings of Machine Learning Research*, pages 6105–6114. PMLR, 09–15 Jun 2019. 2

- [32] M. Tan, R. Pang, and Q. V. Le. Efficientdet: Scalable and efficient object detection. In *2020 IEEE/CVF Conference on Computer Vision and Pattern Recognition (CVPR)*, pages 10778–10787, 2020. [2](#)
- [33] Alexey Trekin, German Novikov, Georgy Potapov, Vladimir Ignatiev, and Evgeny Burnaev. Satellite imagery analysis for operational damage assessment in emergency situations. *CoRR*, abs/1803.00397, 2018. [2](#)
- [34] S. Xie, R. Girshick, P. Dollár, Z. Tu, and K. He. Aggregated residual transformations for deep neural networks. In *2017 IEEE Conference on Computer Vision and Pattern Recognition (CVPR)*, pages 5987–5995, 2017. [2](#)
- [35] S. Yun, D. Han, S. Chun, S. J. Oh, Y. Yoo, and J. Choe. Cutmix: Regularization strategy to train strong classifiers with localizable features. In *2019 IEEE/CVF International Conference on Computer Vision (ICCV)*, pages 6022–6031, 2019. [3](#), [5](#)
- [36] Hongyi Zhang, Moustapha Cisse, Yann N. Dauphin, and David Lopez-Paz. mixup: Beyond empirical risk minimization. In *International Conference on Learning Representations*, 2018. [5](#)
- [37] H. Zhao, J. Shi, X. Qi, X. Wang, and J. Jia. Pyramid scene parsing network. In *2017 IEEE Conference on Computer Vision and Pattern Recognition (CVPR)*, pages 6230–6239, 2017. [1](#), [5](#)
- [38] Kang Zhao, Jungwon Kang, Jaewook Jung, and Gunho Sohn. Building extraction from satellite images using mask r-cnn with building boundary regularization. In *Proceedings of the IEEE Conference on Computer Vision and Pattern Recognition (CVPR) Workshops*, June 2018. [2](#)